

# Dissipation-Induced Threshold on Integrability Footprints

Rodrigo M. C. Pereira,<sup>1,\*</sup> Nadir Samos Sáenz de Buruaga,<sup>1</sup> Kristian Wold,<sup>2,3</sup> Lucas Sá,<sup>4</sup> Sergey Denisov,<sup>2,3</sup> and Pedro Ribeiro<sup>1,5,†</sup>

<sup>1</sup>*CeFEMA-LaPMET, Physics Department, Instituto Superior Técnico, Universidade de Lisboa, 1049-001 Lisboa, Portugal*

<sup>2</sup>*Department of Computer Science, OsloMet – Oslo Metropolitan University, N-0130 Oslo, Norway*

<sup>3</sup>*NordSTAR – Nordic Center for Sustainable and Trustworthy AI Research, N-0166 Oslo, Norway*

<sup>4</sup>*TCM Group, Cavendish Laboratory, University of Cambridge, JJ Thomson Avenue, Cambridge CB3 0HE, UK*

<sup>5</sup>*Beijing Computational Science Research Center, Beijing 100193, China*

The presence of a dissipative environment disrupts the unitary spectrum of dynamical quantum maps. Nevertheless, key features of the underlying unitary dynamics—such as their integrable or chaotic nature—are not immediately erased by dissipation. To investigate this, we model dissipation as a convex combination of a unitary evolution and a random Kraus map, and study how signatures of integrability fade as dissipation strength increases. Our analysis shows that in the weakly dissipative regime, the complex eigenvalue spectrum organizes into well-defined, high-density clusters. We estimate the critical dissipation threshold beyond which these clusters disappear, rendering the dynamics indistinguishable from chaotic evolution. This threshold depends only on the number of spectral clusters and the rank of the random Kraus operator. To characterize this transition, we introduce the eigenvalue angular velocity as a diagnostic of integrability loss. We illustrate our findings through several integrable quantum circuits, including the dissipative quantum Fourier transform. Our results provide a quantitative picture of how noise gradually erases the footprints of integrability in open quantum systems.

*Introduction.*—The study of quantum chaos has gained renewed attention due to its relevance in various areas, including the non-equilibrium dynamics of many-body quantum systems and quantum information processing [1–4].

In closed quantum systems, spectral analysis is widely used to identify chaotic behavior [5]. A key conjecture states that the level statistics of integrable systems follow a Poisson distribution [6], while chaotic systems exhibit level statistics described by random matrix theory [7]. The hallmark of integrable dynamics is level clustering, where the probability density is highest at zero spacing. In contrast, chaotic systems display level repulsion, with the probability density vanishing at small spacings. Even though there is not yet rigorous proof, these statements are strongly supported by several numerical studies [5]. It has also been shown that even small perturbations can induce chaos in the thermodynamic limit, thus breaking integrability [8].

Sampling random unitaries according to the Haar measure on the unitary group, that is, from the circular unitary ensemble (CUE), reliably leads to chaotic spectral statistics. Meanwhile, many physically relevant models remain integrable, such as classical spin chains and free-fermion systems. In the context of quantum information, the latter are also known as matchgate circuits—quantum circuits that emulate the dynamics of non-interacting fermions and can be efficiently simulated

on a classical computer [9–11]. Another highly structured gate set that lacks universal dynamics is the Clifford group. Clifford circuits can be simulated in polynomial time using the stabilizer formalism [12, 13], making them useful in quantum many-body physics and the benchmark of quantum computers [14–17].

Since no real quantum system is perfectly isolated, understanding how chaos and integrability manifest in open quantum systems is essential. In open systems, evolution is governed by non-unitary operators, leading to decoherence and dissipation as information is lost to the environment. Despite this, spectral statistics remain a powerful tool for diagnosing chaotic behavior. Level spacing distributions provide insight into the nature of the system: integrable systems exhibit statistics described by a two-dimensional Poisson process, whereas chaotic systems follow the Ginibre unitary ensemble (GinUE) distribution [18–20]. Other measures, such as complex spacing ratios [21–23], further characterize this distinction: integrable systems yield uniformly distributed points on the unit circle, whereas chaotic systems form a distinctive bitten-doughnut shape.

Dissipation is expected to impact integrable unitary dynamics, eventually leading to universal dissipative behavior. However, the extent to which integrable features persist under generic dissipation channels remains an open question. In this work, we seek to quantify how hallmarks of integrability—such as level clustering—gradually fade as dissipation increases. We model the open-system dynamics as a convex combination of the original unitary map and a random Kraus operator, with the rank of the operator corresponding to the number

\* [rodrigo.m.c.pereira.6@tecnico.ulisboa.pt](mailto:rodrigo.m.c.pereira.6@tecnico.ulisboa.pt)

† [ribeiro.pedro@tecnico.ulisboa.pt](mailto:ribeiro.pedro@tecnico.ulisboa.pt)

of dissipative channels. Interestingly, while conventional measures such as quantum fidelity fail to detect the erosion of integrable behavior, spectral diagnostics offer a more sensitive and intuitive probe. To formalize this spectral signature, we introduce the eigenvalue angular velocity, which captures the impact of dissipation on integrable dynamics. Our results show that level clustering, a defining characteristic of integrability, remains robust against weak dissipation.

The main contribution of this study is the identification of a universal relationship governing the critical dissipation strength beyond which spectral clustering disappears. This critical dissipation depends on both the number of clusters in the unitary map and the rank of the dissipative channel. We derive an analytical expression that accurately approximates the numerical results. Additional details on the numerical methods and further supporting details are provided in the Supplemental Material (SM) [24].

*Diluted unitary.*—We consider a quantum map that deviates from an ideal unitary implementation due to random interactions with the environment. Following the approach in Ref. [25], we define

$$\Phi_M = (1 - \kappa)U_M \otimes U_M^* + \kappa \sum_{j=1}^r K_j \otimes K_j^*, \quad (1)$$

where  $\kappa \in [0, 1]$  controls the dissipation strength. When  $\kappa = 0$ , the evolution is purely unitary, whereas  $\kappa = 1$  corresponds to a random rank- $r$  Kraus map, whose operators satisfy  $\sum_{j=1}^r K_j^\dagger K_j = I$ . Here,  $U_M$  and  $K_j$  are  $d \times d$  matrices, the rank of the Kraus operators is constrained by  $1 \leq r \leq d^2 - 1$ , and the subscript  $M$  on  $U_M$  denotes the ensemble from which the unitary is sampled. We refer to  $\Phi_M$  as a *diluted unitary*.

We aim to investigate the impact of dissipation on various maps exhibiting chaotic and distinct regular dynamics, as well as to identify measures that distinguish their behaviors and responses to the loss of unitarity. Notably, the differences between the models arise solely from the choice of the unitary operator; the Kraus map that mimics the complex noisy environment is sampled by generating a large  $rd \times rd$  unitary random matrix  $W \in \text{CUE}$  and chopping the first  $d$  columns into  $r$  blocks [26], which we take to be the Kraus operators,  $(K_j)_{ab} = W_{(j-1)d+a,b}$ , with  $a, b = 1, \dots, d$ ,  $j = 1, \dots, r$ . The unitarity of  $W$  ensures that the constraint on the Kraus operators is satisfied.

We analyze a chaotic case, with  $U_M$  taken to be a random matrix sampled from the CUE, and three integrable models: (i) an operator from the Clifford group sampled uniformly as in Ref. [27], (ii) an integrable periodically driven (or Floquet) spin-1/2 chain based on Ref. [28], and (iii) a random matrix implementing free-fermion dynamics, i.e., a random matchgate circuit. These systems are defined on  $L$  sites, such that the Hilbert space dimension is  $d = 2^L$ . A detailed description of  $U_M$  and the sampling procedure for all cases can be found in SM A.

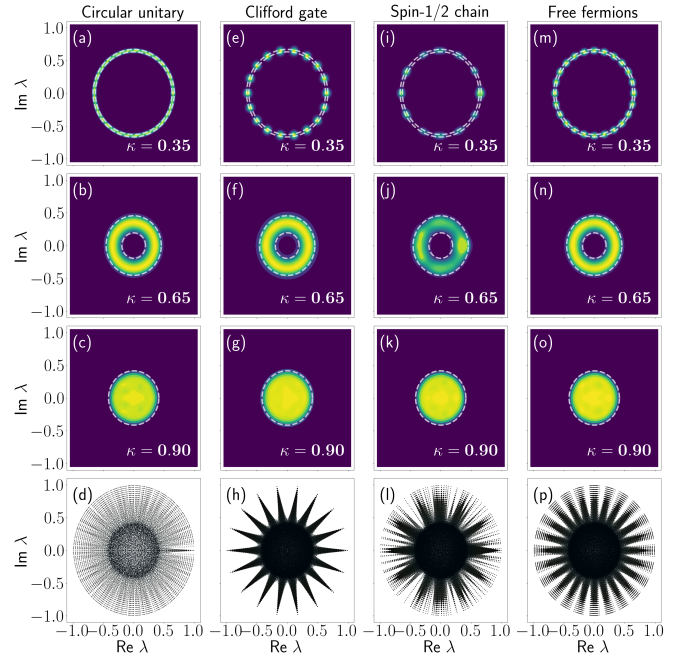


Figure 1. Spectrum of the quantum maps in Eq. (1) for  $L = 6$  and  $r = 5$ . Each column represents a different model based on the ensemble of the unitary circuit, indicated on top. The first three rows depict the eigenvalue density for the indicated value of  $\kappa$ . The white dashed lines are the circumferences with inner and outer radii given by Eq. (2). The spectrum of the chaotic model in the first column is characterized by a single R-D transition, whereas the integrable models in the remaining columns have an additional C-R transition. The last row depicts the trajectories of the eigenvalues with increasing  $\kappa$ .

*Integrability footprints.*—As a first approach, we analyze the quantum fidelity between a clean pure state  $|\Psi\rangle$  and its actual noisy realization  $\rho$ ,  $\mathcal{F} = \langle \Psi | \rho | \Psi \rangle$ , for a random quantum circuit. Each layer comprises a random map of the form Eq. (1) for a specific choice of ensemble and constant dissipation strength  $\kappa$ . For each time step, we sample a new random diluted unitary. Since the Kraus operators are obtained from a Haar-random matrix, they inherit the left-right invariance property. Consequently, the average fidelity is fully determined by the statistics of the Kraus operators, and the specific unitary ensemble becomes irrelevant. Therefore, this measure is not able to distinguish the different models, and therefore the loss of integrability of the systems. For a detailed discussion, see SM B.

We now turn our attention to the spectral properties of the maps. Figure 1 presents the spectra of the four models introduced previously. Each column corresponds to a different model, with the first three rows displaying the eigenvalue distributions for a given dissipation strength  $\kappa$ , and the last row illustrating the eigenvalue trajectories in the complex plane as  $\kappa$  increases. While there is always at least one stationary state with eigenvalue 1, its contribution to the eigenvalue density is negligible in the large-system-size limit, so it is not represented.

The chaotic model in the first column was previously analyzed in Ref. [25] and is characterized by a uniform angular distribution of eigenvalues within a ring of outer ( $R_+$ ) and inner ( $R_-$ ) radii:

$$R_{\pm} = \frac{1}{\sqrt{r}} \sqrt{(1 - \kappa)^2 r \pm \kappa^2}. \quad (2)$$

This behavior is illustrated in Figs. 1 (a) and (b). At the critical value

$$\kappa_{\text{R-D}} = \frac{1}{1 + 1/\sqrt{r}}, \quad (3)$$

where  $R_- = 0$ , a ring-to-disk (R-D) transition occurs, as shown in Fig. 1 (c).

When considering a unitary operation with degeneracies, as is typical for regular dynamics due to level clustering, there are areas with a significantly high eigenvalue density and regions where it vanishes. We call these structures *clusters*, which can be seen in Figs. 1 (e), (i) and (m). These clusters persist up to a critical value  $\kappa_{\text{C-R}}$ . Beyond this threshold, the initial structure of the unitary map is no longer discernible, and a cluster-to-ring (C-R) transition occurs, as illustrated in Figs. 1 (f), (j) and (n). The resulting ring has approximately the same inner and outer radii given in Eq. (2). Similarly to the chaotic case, once the inner radius of the ring vanishes, an R-D transition takes place at the same critical value  $\kappa_{\text{R-D}}$ , as shown in Figs. 1 (g), (k) and (o). This transition is discussed further in SM C.

The eigenvalue trajectories of the chaotic model in Fig. 1 (d) suggest that, for small values of  $\kappa$ , eigenvalues exhibit predominantly radial motion due to level repulsion, with no significant angular displacement. However, for the integrable maps in Figs. 1 (h), (l) and (p), this is not the case, as dissipation lifts degeneracies and induces angular variations.

*Eigenvalue angular velocity.*—Quantifying angular variation is thus essential for distinguishing chaotic from integrable systems. Given an eigenvalue at a certain dissipation strength  $\kappa$ , expressed as  $\lambda(\kappa) = s(\kappa)e^{i\theta(\kappa)}$ , we define its angular velocity as

$$v_{\theta}(\kappa) \equiv \left| \frac{d\theta(\kappa)}{d\kappa} \right| \approx \left| \frac{\theta(\kappa + d\kappa) - \theta(\kappa)}{d\kappa} \right|. \quad (4)$$

To describe the overall spectral behavior, we consider the mean angular velocity,  $\bar{v}_{\theta}$ , averaged over all eigenvalues. In the small  $\kappa$  limit, this quantity is expected to vanish for chaotic unitaries but remain finite for integrable ones. As  $\kappa$  increases, the clusters of eigenvalues expand and merge, eventually forming a ring. At this stage, the original nature of the unitary operator is no longer discernible. Consequently, for  $\kappa > \kappa_{\text{C-R}}$ , chaotic and integrable models should exhibit similar angular velocities.

Before numerically analyzing the angular velocity, we derive an estimate for the critical value  $\kappa_{\text{C-R}}$ , which we

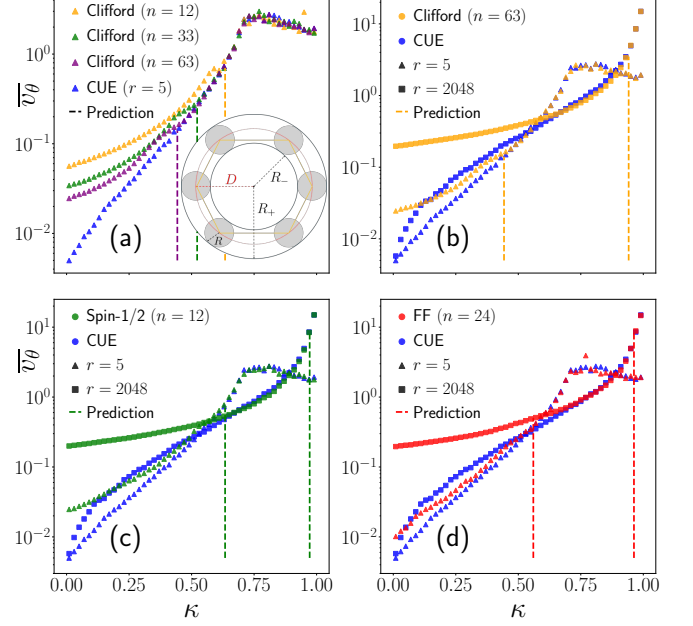


Figure 2. Mean eigenvalue angular velocity as a function of dissipation strength, for distinct models and  $L = 6$ . The C-R transition occurs at the critical value for which the curve of an integrable model starts overlapping with the chaotic one. The dashed lines correspond to the estimate of the transition value  $\kappa_{\text{C-R}}$  given by Eq. (6). (a): CUE model and random Clifford operators with different number of clusters  $n$ , both with  $r = 5$ . (b)–(d): CUE model and the (b) Clifford, (c) integrable spin-1/2, and (d) free-fermion models, for  $r = 5$  and 2048. The inset of (a) depicts the geometric scheme for the derivation of Eq. (5).

identify as the value of dissipation for which clusters occupy the same area as the ring. Consider the idealized case where each cluster forms a perfect circle of radius  $R$ , with centers arranged in a regular polygon with  $n$  vertices (corresponding to the number of clusters) at a distance  $D$  from the origin. This geometric configuration is illustrated in the inset of Fig. 2 (a) for  $n = 6$ . Near the C-R transition, the clusters can be assumed within a ring characterized by  $R = (R_+ - R_-)/2$  and  $D = (R_+ + R_-)/2$ , with their centers in the middle of the ring. The total area covered by the ring is  $\pi(R_+^2 - R_-^2) = 2\pi\kappa^2/r$ , whereas the total area occupied by the clusters is  $n\pi R^2$ . The transition occurs when these two areas are the same, leading to the condition

$$\frac{2\kappa^2}{r} = n \frac{(R_+ - R_-)^2}{4} \quad (5)$$

Solving this equation provides an estimate for  $\kappa_{\text{C-R}}$ , given by

$$\kappa_{\text{C-R}} = \frac{1}{1 + \frac{f(n)}{\sqrt{r}}}, \quad (6)$$

where  $f(n) = \sqrt{2/n + n/8}$ . This expression reduces to

Eq. (3) in the case where  $n = 4$ . For sufficiently large  $n$ ,  $f(n) \approx \sqrt{n}/8$ .

The transition value mainly depends on the ratio  $n/r$  and exhibits two limiting behaviors. When  $n \gg r$ , the transition occurs at smaller values of  $\kappa$  as the number of clusters increases, meaning that  $\kappa_{\text{C-R}} < \kappa_{\text{R-D}}$ . In contrast, when  $n \ll r$ , the transition value approaches unity, meaning that it coincides with the R-D transition, i.e.,  $\kappa_{\text{C-R}} \rightarrow \kappa_{\text{R-D}}$ .

It is worth highlighting a somewhat counterintuitive observation: dilute-unitary maps that model environments with many dissipative channels (corresponding to a higher rank  $r$ ) can preserve unitary spectral features under stronger dissipation compared to their low-rank counterparts. In particular, increasing  $r$  delays the R-D transition to higher values of the dissipation strength  $\kappa$  [see Eq. (3)]. Our results further show that higher-rank maps also sustain integrable signatures up to larger values of  $\kappa$ , whereas concentrating dissipation into a small number of channels proves to be more detrimental to integrable spectral features.

To compute the average angular velocity numerically, we construct the quantum map defined in Eq. (1) for two close values of  $\kappa$  separated by  $d\kappa = \kappa/1000$ . By identifying the nearest-neighbor eigenvalues between the two maps, we track their trajectories and compute the angular velocity for each eigenvalue using Eq. (4), averaging over the entire spectrum. To improve numerical stability, real eigenvalues were discarded since their nearest neighbors were often misidentified, leading to abrupt fluctuations in velocity.

Figure 2 (a) presents numerical results for the Clifford model with different numbers of clusters  $n$  and fixed rank  $r = 5$ . As a different number of clusters may arise from randomly sampling Clifford circuits with the same size and depth, we postselect one that yields exactly  $n$  clusters. Beyond a threshold  $\kappa_{\text{C-R}}$ , the angular velocities converge to that of the chaotic model, indicating that  $\overline{v_\theta}$  successfully signals the C-R transition. Moreover, systems with fewer clusters, meaning a higher degree of degeneracy, exhibit larger  $\kappa_{\text{C-R}}$ , in agreement with Eq. (6).

Figures 2 (b)–(d) depict the average angular velocity for the Clifford, integrable spin-1/2, and free-fermion models, respectively, for a fixed number of clusters and two different values of the rank  $r$ . The results confirm that in the large- $r$  limit, the transition value approaches unity, further supporting the evidence that increasing the rank preserves integrability up to higher values of  $\kappa$ .

*Special case of the QFT.*—An example of an integrable unitary with a highly structured spectrum is the quantum Fourier transform (QFT) [29], an algorithm that can be efficiently implemented in a quantum computer. For an  $L$ -qubit system, the matrix elements of its unitary operator are given by  $(U_{\text{QFT}})_{jk} = 1/\sqrt{L} e^{2\pi i jk/L}$ . For all system sizes, this operator has a fixed number  $n = 4$  of distinct eigenvalues,  $\pm 1, \pm i$ .

In Fig. 3 (a), we depict the spectrum of the diluted unitary map with  $U_M = U_{\text{QFT}}$ , for  $\kappa = 0.75$  and  $r = 5$ .

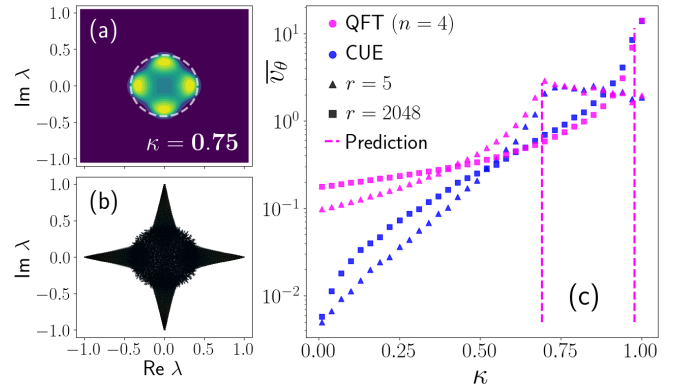


Figure 3. (a) Eigenvalue density for  $U_M = U_{\text{QFT}}$  with  $L = 6$ ,  $r = 5$ , and  $\kappa = 0.75$ . (b) Eigenvalue trajectories with increasing  $\kappa$  for fixed  $r = 5$ . (c) Mean eigenvalue angular velocity for the CUE and QFT models for  $r = 5$  and 2048. The dashed lines correspond to the estimate of the transition value  $\kappa_{\text{C-R}}$  given by Eq. (6).

Figure 3 (b) shows the trajectories of the eigenvalues as dissipation increases, leading them to converge toward the center until they form a disk. Because the number of clusters is small, distinguishing two separate transitions becomes challenging. Instead, this model appears to exhibit a single cluster-to-disk (C-D) transition, as  $\kappa_{\text{C-R}}$  in Eq. (6) reduces to  $\kappa_{\text{R-D}}$  in Eq. (3) for  $n = 4$ . It is worth noting that, according to Eq. (3), the R-D transition is expected to occur at  $\kappa_{\text{R-D}} \approx 0.69$  for  $r = 5$ . However, Fig. 3 (a) shows that the disk still does not homogeneously cover the entire circle. This indicates that traces of the unitary structure are still partially preserved, as the limited number of clusters prevents a uniformly distributed ring. Nevertheless, Fig. 3 (c) shows that this C-D transition marks the threshold beyond which the angular velocity behavior aligns with that of random maps.

*Conclusion.*—We have shown that the spectrum of integrable systems weakly coupled to an environment exhibits distinct eigenvalue clustering. We demonstrated that dissipation gradually erodes these spectral features that signal the underlying regular dynamics in quantum systems. By analyzing the complex eigenvalue spectra of diluted unitary maps, we identified two key transitions—cluster-to-ring and ring-to-disk—which signal the breakdown of integrable dynamics.

We introduced the eigenvalue angular velocity as a sensitive diagnostic of the cluster-to-ring transition, providing a quantitative estimate for the critical dissipation threshold. This threshold depends universally on the number of clusters and the rank of the dissipative channel. Our findings apply across a variety of integrable systems, including Clifford circuits, spin chains, and the quantum Fourier transform.

These results shed light on how dissipation governs the loss of integrability in open quantum systems, offering a concrete proxy for when structured, integrable dynamics give way to universal, chaotic behavior. In typical



dynamical systems, the number of spectral clusters—linked to conserved quantities—is expected to grow exponentially with system size, while the number of dissipative channels generally increases only algebraically due to the local nature of most environmental couplings. As a result, in the thermodynamic limit, even exponentially small dissipation is sufficient to erase integrability signatures. However, this is not a universal rule: certain systems, such as the quantum Fourier transform, exhibit fixed spectral structures that challenge this scaling. Finally, the strong dependence of the transition on the rank of the dissipative channel suggests that coherence in quantum simulations and computations could be pre-

served longer by engineering environments with higher-rank noise, opening new avenues for mitigating dissipative effects.

*Acknowledgments.*—This work was realized within the DQUANT QuantEra II Programme was supported by the National Science Centre, Poland, under the project 2021/03/Y/ST2/00193, and by FCT-Portugal Grant Agreement No. 101017733.<sup>1</sup> It received funding from the European Union’s Horizon 2020 research and innovation programme under Grant Agreement No 101017733. PR, NS, and RP acknowledge further support from FCT-Portugal through Grant No. UID/CTM/04540/2020. LS was supported by a Research Fellowship from the Royal Commission for the Exhibition of 1851.

- 
- [1] B. Kobrin, Z. Yang, G. D. Kahanamoku-Meyer, C. T. Olund, J. E. Moore, D. Stanford, and N. Y. Yao, Many-Body Chaos in the Sachdev-Ye-Kitaev Model, *Phys. Rev. Lett.* **126**, 030602 (2021).
  - [2] E. Lantagne-Hurtubise, S. Plugge, O. Can, and M. Franz, Diagnosing quantum chaos in many-body systems using entanglement as a resource, *Phys. Rev. Res.* **2**, 013254 (2020).
  - [3] L. M. Sieberer, T. Olsacher, A. Elben, M. Heyl, P. Hauke, F. Haake, and P. Zoller, Digital quantum simulation, Trotter errors, and quantum chaos of the kicked top, *npj Quantum Inf.* **5**, 78 (2019).
  - [4] A. Rath, C. Branciard, A. Minguzzi, and B. Vermersch, Quantum Fisher Information from Randomized Measurements, *Phys. Rev. Lett.* **127**, 260501 (2021).
  - [5] F. Haake, *Quantum Signatures of Chaos* (Springer, Berlin, 2010).
  - [6] M. V. Berry and M. Tabor, Level clustering in the regular spectrum, *Proc. R. Soc. Lond. A* **356**, 375 (1977).
  - [7] O. Bohigas, M. J. Giannoni, and C. Schmit, Characterization of Chaotic Quantum Spectra and Universality of Level Fluctuation Laws, *Phys. Rev. Lett.* **52**, 1 (1984).
  - [8] D. A. Rabson, B. N. Narozhny, and A. J. Millis, Crossover from Poisson to Wigner-Dyson level statistics in spin chains with integrability breaking, *Phys. Rev. B* **69**, 054403 (2004).
  - [9] L. G. Valiant, Quantum computers that can be simulated classically in polynomial time (ACM, New York, 2001) p. 114.
  - [10] B. M. Terhal and D. P. DiVincenzo, Classical simulation of noninteracting-fermion quantum circuits, *Phys. Rev. A* **65**, 032325 (2002).
  - [11] R. Jozsa and A. Miyake, Matchgates and classical simulation of quantum circuits, *Proc. R. Soc. Lond. A* **464**, 3089 (2008).
  - [12] D. Gottesman, The Heisenberg representation of quantum computers, *arXiv:quant-ph/9807006* (1998).
  - [13] S. Aaronson and D. Gottesman, Improved simulation of stabilizer circuits, *Phys. Rev. A* **70**, 052328 (2004).
  - [14] Y. Li, X. Chen, and M. P. A. Fisher, Quantum Zeno effect and the many-body entanglement transition, *Phys. Rev. B* **98**, 205136 (2018).
  - [15] E. Magesan, J. M. Gambetta, and J. Emerson, Scalable and Robust Randomized Benchmarking of Quantum Processes, *Phys. Rev. Lett.* **106**, 180504 (2011).
  - [16] E. Onorati, A. H. Werner, and J. Eisert, Randomized Benchmarking for Individual Quantum Gates, *Phys. Rev. Lett.* **123**, 060501 (2019).
  - [17] J. Helsen, I. Roth, E. Onorati, A. Werner, and J. Eisert, General Framework for Randomized Benchmarking, *PRX Quantum* **3**, 020357 (2022).
  - [18] J. Ginibre, Statistical ensembles of complex, quaternion, and real matrices, *J. Math. Phys.* **6**, 440 (1965).
  - [19] R. Grobe, F. Haake, and H.-J. Sommers, Quantum Distinction of Regular and Chaotic Dissipative Motion, *Phys. Rev. Lett.* **61**, 1899 (1988).
  - [20] G. Akemann, M. Kieburg, A. Mielke, and T. Prosen, Universal Signature from Integrability to Chaos in Dissipative Open Quantum Systems, *Phys. Rev. Lett.* **123**, 254101 (2019).
  - [21] L. Sá, P. Ribeiro, and T. Prosen, Complex Spacing Ratios: A Signature of Dissipative Quantum Chaos, *Phys. Rev. X* **10**, 021019 (2020).
  - [22] A. M. García-García, L. Sá, and J. J. M. Verbaarschot, Symmetry Classification and Universality in Non-Hermitian Many-Body Quantum Chaos by the Sachdev-Ye-Kitaev Model, *Phys. Rev. X* **12**, 021040 (2022).
  - [23] Álvaro Rubio-García, R. A. Molina, and J. Dukelsky, From integrability to chaos in quantum Liouvillians, *SciPost Phys. Core* **5**, 026 (2022).
  - [24] See the Supplemental Material for details of the models and their numerical sampling, the fidelity decay, and the ring-to-disk transition.
  - [25] L. Sá, P. Ribeiro, T. Can, and T. Prosen, Spectral transitions and universal steady states in random Kraus maps and circuits, *Phys. Rev. B* **102**, 134310 (2020).
  - [26] W. Bruzda, V. Cappellini, H.-J. Sommers, and K. Życzkowski, Random quantum operations, *Phys. Lett. A* **373**, 320 (2009).
  - [27] E. Van Den Berg, A simple method for sampling random Clifford operators, in *2021 IEEE International Conference on Quantum Computing and Engineering (QCE)* (IEEE, Los Alamitos, CA, USA, 2021) pp. 54–59.

<sup>1</sup> <https://doi.org/10.54499/QuantERA/0003/2021>

- [28] M. Vanicat, L. Zadnik, and T. Prosen, Integrable Trotterization: Local Conservation Laws and Boundary Driving, *Phys. Rev. Lett.* **121**, 030606 (2018).
- [29] D. Coppersmith, An approximate fourier transform useful in quantum factoring, [arXiv:quant-ph/0201067](#) (2002).
- [30] F. Mezzadri, How to generate random matrices from the classical compact groups, *Not. Am. Math. Soc.* **54**, 592 (2007).
- [31] L. Faddeev, How algebraic Bethe ansatz works for integrable model, [arXiv:hep-th/9605187](#) (1996).
- [32] R. Baxter, Asymptotically degenerate maximum eigenvalues of the eight-vertex model transfer matrix and interfacial tension, *J. Stat. Phys.* **8**, 25 (1973).
- [33] M. Jimbo, A q-difference analogue of  $U(g)$  and the Yang-Baxter equation, *Lett. Math. Phys.* **10**, 63 (1985).
- [34] R. Somma, G. Ortiz, J. E. Gubernatis, E. Knill, and R. Laflamme, Simulating physical phenomena by quantum networks, *Phys. Rev. A* **65**, 042323 (2002).
- [35] M. A. Nielsen, [The fermionic canonical commutation relations and the jordan-wigner transform](#) (2005).
- [36] S. M. B. Collins and J. Novak, The Weingarten Calculus, *Not. Am. Math. Soc.* **69**, 734 (2022).

# Supplemental Material for Dissipation-Induced Threshold on Integrability Footprints

## Appendix A: Sampling methods

In this section, we explain the numerical methods used to generate the random matrices described in the main text.

### 1. Circular unitary ensemble

The algorithm to generate a random matrix from the CUE is as follows [30]: we sample a  $d \times d$  random matrix  $Z$  from the GinUE, and perform any QR decomposition algorithm such that  $Z = QR$ . Then, write the diagonal matrix  $\Lambda = \text{diag}(R_{11}/|R_{11}|, \dots, R_{dd}/|R_{dd}|)$ , where  $R_{ii}$  is the  $i$ -th diagonal element of  $R$ . Finally, we realize the transformation  $Q \rightarrow Q\Lambda$ . The new  $Q$  is Haar-distributed and therefore belongs to the CUE.

### 2. Kraus operators

Let us now look at how to sample the  $r$  Kraus operators  $K_j$ . A way to proceed is by following Ref. [26]. To that end, we sample a matrix  $W \in \text{CUE}$  with dimensions  $rd \times rd$ . Then, the Kraus operators correspond to the first (or any) block column of  $d \times d$  matrices. The condition  $\sum_{j=1}^r K_j^\dagger K_j = \mathbb{I}$  is satisfied due to the orthogonality of the columns of  $W$ . However, this algorithm is computationally inefficient since it only uses the information of one block column of an enlarged matrix. Thus, in the numerics of the paper, we alternatively considered the following algorithm.

We begin by generating an  $rd \times d$  random matrix from the GinUE, perform a  $QR$  decomposition, and extract the rectangular matrix  $Q$ , which is also  $rd \times d$ . Then we perform the transformation  $Q \rightarrow Q\Lambda$ , with  $\Lambda = \text{diag}(R_{11}/|R_{11}|, \dots, R_{dd}/|R_{dd}|)$ , necessary to obtain the correct eigenvalue density distribution. Finally, we take  $d$  consecutive rows and truncate the matrix dividing it into  $r$   $d \times d$  matrices:

$$Q = \left( \begin{array}{ccc|ccc|ccc} Q_{1,1} & \cdots & Q_{1,d} & & & & & & \\ \vdots & & \ddots & & & & & & \\ Q_{d,1} & \cdots & Q_{d,d} & & & & & & \\ \hline Q_{d+1,1} & \cdots & Q_{d+1,d} & & & & & & \\ \vdots & & \ddots & & & & & & \\ Q_{2d,1} & \cdots & Q_{2d,d} & & & & & & \\ \hline \vdots & & \ddots & & & & & & \\ Q_{rd,1} & \cdots & Q_{rd,d} & & & & & & \end{array} \right) \left. \begin{array}{l} \\ \\ \\ \\ \end{array} \right\} \begin{array}{l} K_1 \\ \\ K_2 \\ \\ \vdots \end{array} \quad (\text{A1})$$

The condition  $\sum_{j=1}^r K_j^\dagger K_j = \mathbb{I}$  is automatically met since  $Q^\dagger Q = \mathbb{I}$ . More explicitly:

$$(Q^\dagger Q)_{\alpha\alpha'} = \sum_{(\beta\gamma)=1}^{rd} (Q^\dagger)_{\alpha(\beta\gamma)} Q_{(\beta\gamma)\alpha'} = \sum_{\beta=1}^r \sum_{\gamma=1}^d (K_\beta^\dagger)_{\alpha\gamma} (K_\beta)_{\gamma\alpha'} = \sum_{\beta=1}^r (K_\beta^\dagger K_\beta)_{\alpha\alpha'} = \left( \sum_{\beta=1}^r K_\beta^\dagger K_\beta \right)_{\alpha\alpha'} = \mathbb{I}_{\alpha\alpha'}. \quad (\text{A2})$$

### 3. Clifford operator

We uniformly sample a Clifford gate according to Ref. [27], which can be done efficiently, i.e., in polynomial time. The algorithm takes advantage of the tableau representation of a Clifford operator  $\mathcal{C}$  [13], where acting with Clifford operations translates into actions on the tableau, e.g., a Hadamard gate is responsible for exchanging columns.

It is important to notice that, since we are interested in the full map, we need to compute a  $2^L \times 2^L$  matrix. Thus, even though the sampling is classically done in polynomial time, the building of the matrix itself scales exponentially with system size and is no longer computationally efficient.

#### 4. Integrable spin-1/2 chain

We will consider the work of Ref. [28], which introduces a spin-1/2 chain that is integrable in the Bethe-ansatz sense [31]. This model corresponds to taking a brickwall circuit with periodic boundary conditions, where each two-qubit unitary  $u_{j,j+1}$  acting on qubits  $j$  and  $j+1$  is taken to be the  $\check{R}$  matrix<sup>2</sup> of the XXX model [31],

$$u_{j,j+1} = \check{R}_{j,j+1}(\delta), \quad \check{R}(\delta) = \frac{\mathbb{I} + i\delta P}{\mathbb{I} + i\delta}, \quad (\text{A3})$$

where the real parameter  $\delta$  is a spin coupling constant and  $P_{j,j+1} = 1/2(\mathbb{I} + \boldsymbol{\sigma}_j \cdot \boldsymbol{\sigma}_{j+1})$ , with  $\boldsymbol{\sigma} = (\sigma^x, \sigma^y, \sigma^z)$  a vector with the Pauli matrices. A one-layer unitary matrix  $\mathcal{U}$  acting on  $L$  qubits is obtained by a two-step operation, first consisting of the action of  $u$  over the odd-even sites, and then the action over the even-odd sites,

$$\mathcal{U} = \mathcal{U}_{\text{even}} \mathcal{U}_{\text{odd}} = \prod_{j=1}^{L/2} u_{2j-1,2j} \prod_{k=1}^{L/2} u_{2k,2k+1}, \quad (\text{A4})$$

where we must restrict to even  $L$  and the sites 1 and  $L+1$  are the same, as imposed by periodic boundary conditions. Let us call  $\mathcal{U}_t$  the operation realized in the layer  $t$ . The total unitary  $U$  corresponds to multiplying the matrices over  $T$  layers:

$$U = \prod_{t=1}^T \mathcal{U}_t. \quad (\text{A5})$$

To randomly sample a unitary matrix  $\mathcal{U}_t$ , we obtain a random  $\theta \in [0, \pi]$  and calculate  $\delta = \tan \theta$ , allowing us to compute a random real number, even though not uniformly. This parameterization satisfies the relation  $\check{R}(\tan \theta) \check{R}(\tan \theta') = \check{R}[\tan(\theta + \theta')]$ .

For numerical simulations, we fixed the number of layers in  $T = L$  and considered the case where each layer consists of the same operation, i.e.  $\mathcal{U}_t \equiv \mathcal{U}$ , such that the total matrix corresponds to  $U = \mathcal{U}^L$ . With this method, we only sample  $\theta$  once.

#### 5. Free fermions

The most general quadratic fermionic Hamiltonian can be written as

$$H_{FF} = \sum_{j,k=1}^L 2h_{jk} c_j^\dagger c_k + \sum_{j,k=1}^L \left( \Delta_{jk} c_j^\dagger c_k^\dagger - \Delta_{jk}^* c_j c_k \right), \quad (\text{A6})$$

where  $L$  is the number of sites. The first term describes the dynamics of the fermions within the chain and the last two refer to the creation and annihilation of pairs, which causes the non-conservation of the number of particles. However, parity is conserved, i.e., whether the number of particles is even or odd never changes.

Defining the Nambu vector  $C = (c_1 \dots c_L c_1^\dagger \dots c_L^\dagger)^T$  we can write Eq. (A6) as

$$H_{FF} = C^\dagger \mathbf{H} C, \text{ with } \mathbf{H} = \begin{pmatrix} h & \Delta \\ -\Delta^* & -h^* \end{pmatrix}, \quad (\text{A7})$$

where  $\mathbf{H}$  is the single particle Hamiltonian, and  $h = h^\dagger$  and  $\Delta = -\Delta^T$  are  $L \times L$  matrices.

---

<sup>2</sup> This matrix corresponds to a solution of the Yang-Baxter equation [32, 33].



We can map fermionic operators onto spin operators through the Jordan-Wigner transformation [34, 35]

$$\begin{aligned} c_m^\dagger &= e^{i\frac{\pi}{2} \sum_{k=1}^{j-1} (1-\sigma_k^z)} \sigma_m^- = S_{1m} \sigma_m^-, \\ c_m &= e^{-i\frac{\pi}{2} \sum_{k=1}^{m-1} (1-\sigma_k^z)} \sigma_m^+ = S_{1m}^\dagger \sigma_m^+, \end{aligned} \quad (\text{A8})$$

which reproduces the correct commutation relations with

$$c_m^\dagger c_m = \frac{1}{2} (1 - \sigma_m^z). \quad (\text{A9})$$

With this definition, the string operator  $S_{ij} = S_{ij}^\dagger = (-1)^{p_{i,j}}$  where  $p_{i,j}$  counts the number of spins  $|-\rangle$  between the  $i$ -th and  $(j-1)$ -th positions. Defining the spinor

$$\Sigma = \begin{pmatrix} \sigma_1^- \\ \vdots \\ \sigma_N^- \\ \sigma_1^+ \\ \vdots \\ \sigma_N^+ \end{pmatrix} = \begin{pmatrix} \sigma^- \\ \sigma^+ \end{pmatrix}, \quad (\text{A10})$$

we can encode the Jordan-Wigner transformation into a  $2L \times 2L$  matrix and write the Nambu vector as

$$C = J\Sigma, \quad J = \begin{pmatrix} \mathbf{0} & \mathbf{S} \\ \mathbf{S} & \mathbf{0} \end{pmatrix}, \quad \mathbf{S} = \text{diag}\{S_{11}, \dots, S_{1N}\}, \quad (\text{A11})$$

where  $S_{ij}$  is the string operator. If we plug Eq. (A11) in Eq. (A7) we obtain the spin first-quantized Hamiltonian

$$H_{FF} = \Sigma^\dagger J H J \Sigma = \Sigma^\dagger \mathbf{H}_{\text{spin}} \Sigma, \quad \mathbf{H}_{\text{spin}} = \begin{pmatrix} -\mathbf{S} \mathbf{h}^* \mathbf{S} & -\mathbf{S} \mathbf{\Delta}^* \mathbf{S} \\ \mathbf{S} \mathbf{\Delta} \mathbf{S} & \mathbf{S} \mathbf{h} \mathbf{S} \end{pmatrix}, \quad (\text{A12})$$

with

$$\mathbf{S} \mathbf{h} \mathbf{S} = \mathbf{h}_{\text{spin}} = \begin{pmatrix} h_{11} & h_{12}(-1)^{p_{12}} & \dots & h_{12}(-1)^{p_{1N}} \\ h_{12}^*(-1)^{p_{12}} & h_{22} & \dots & \vdots \\ \vdots & \vdots & \ddots & h_{N-1N}(-1)^{p_{N-1,N}} \\ h_{12}^*(-1)^{p_{1N}} & \dots & h_{N-1N}^*(-1)^{p_{N-1,N}} & h_{NN} \end{pmatrix} \quad (\text{A13})$$

and

$$\mathbf{S} \mathbf{\Delta} \mathbf{S} = \mathbf{\Delta}_{\text{spin}} = \begin{pmatrix} 0 & \Delta_{12}(-1)^{p_{12}} & \dots & \Delta_{12}(-1)^{p_{1N}} \\ -\Delta_{12}(-1)^{p_{12}} & 0 & \dots & \vdots \\ \vdots & \vdots & \ddots & \Delta_{N-1N}(-1)^{p_{N-1,N}} \\ -\Delta_{12}(-1)^{p_{1N}} & \dots & -\Delta_{N-1N}(-1)^{p_{N-1,N}} & 0 \end{pmatrix}. \quad (\text{A14})$$

We proceed by computing the matrix elements of the many-body Hamiltonian in the many-body basis:

$$\begin{aligned} \sigma^- \mathbf{h}_{\text{spin}} \sigma^+ |\sigma_1, \dots, \sigma_k, \dots, \sigma_l, \dots, \sigma_N\rangle &= \left( \sum_{k=1}^N h_{kk} \sigma_k^- \sigma_k^+ + \sum_{k < l} h_{kl} \sigma_k^- (-1)^{p_{kl}} \sigma_l^+ \right. \\ &\quad \left. + \sum_{k < l} h_{kl}^* \sigma_l^- (-1)^{p_{kl}} \sigma_k^+ \right) |\sigma_1, \dots, \sigma_k, \dots, \sigma_l, \dots, \sigma_N\rangle \\ &= \left( \sum_{k=1}^N h_{kk} \delta_{\sigma_k, -} \right) |\sigma_1, \dots, \sigma_k, \dots, \sigma_l, \dots, \sigma_N\rangle \\ &\quad + \sum_{k < l} h_{kl} \delta_{\sigma_k, +} \delta_{\sigma_l, -} (-1)^{p_{k+1,l}} |\sigma_1, \dots, -, \dots, +, \dots, \sigma_N\rangle \\ &\quad + \sum_{k < l} h_{kl}^* \delta_{\sigma_k, -} \delta_{\sigma_l, +} (-1)^{p_{k+1,l}} |\sigma_1, \dots, +, \dots, -, \dots, \sigma_N\rangle, \end{aligned} \quad (\text{A15})$$

$$\begin{aligned}
-\sigma^+ \mathbf{h}_{\text{spin}}^* \sigma^- |\sigma_1, \dots, \sigma_k, \dots, \sigma_l, \dots, \sigma_N\rangle &= \left( -\sum_{k=1}^N h_{kk} \sigma_k^+ \sigma_k^- - \sum_{k < l} h_{kl}^* \sigma_k^+ (-1)^{p_{kl}} \sigma_l^- \right. \\
&\quad \left. - \sum_{k < l} h_{kl} \sigma_l^+ (-1)^{p_{kl}} \sigma_k^- \right) |\sigma_1, \dots, \sigma_k, \dots, \sigma_l, \dots, \sigma_N\rangle \\
&= -\left( \sum_{k=1}^N h_{kk} \delta_{\sigma_k, +} \right) |\sigma_1, \dots, \sigma_k, \dots, \sigma_l, \dots, \sigma_N\rangle \\
&\quad + \sum_{k < l} h_{kl}^* \delta_{\sigma_k, -} \delta_{\sigma_l, +} (-1)^{p_{k+1, l}} |\sigma_1, \dots, +, \dots, -, \dots, \sigma_N\rangle \\
&\quad + \sum_{k < l} h_{kl} \delta_{\sigma_k, +} \delta_{\sigma_l, -} (-1)^{p_{k+1, l}} |\sigma_1, \dots, -, \dots, +, \dots, \sigma_N\rangle,
\end{aligned} \tag{A16}$$

$$\begin{aligned}
\sigma^- \Delta_{\text{spin}} \sigma^- |\sigma_1, \dots, \sigma_k, \dots, \sigma_l, \dots, \sigma_N\rangle &= \sum_{k < l} \Delta_{kl} \sigma_k^- (-1)^{p_{kl}} \sigma_l^- - \Delta_{kl} \sigma_l^- (-1)^{p_{kl}} \sigma_k^- \Big) |\sigma_1, \dots, \sigma_k, \dots, \sigma_l, \dots, \sigma_N\rangle \\
&= \sum_{k < l} 2\Delta_{kl} \delta_{\sigma_k, +} \delta_{\sigma_l, +} (-1)^{p_{k+1, l}} |\sigma_1, \dots, -, \dots, -, \dots, \sigma_N\rangle,
\end{aligned} \tag{A17}$$

$$\begin{aligned}
-\sigma^+ \Delta_{\text{spin}}^* \sigma^+ |\sigma_1, \dots, \sigma_k, \dots, \sigma_l, \dots, \sigma_N\rangle &= -\sum_{k < l} \Delta_{kl}^* \sigma_k^+ (-1)^{p_{kl}} \sigma_l^+ + \Delta_{kl}^* \sigma_l^+ (-1)^{p_{kl}} \sigma_k^+ \Big) |\sigma_1, \dots, \sigma_k, \dots, \sigma_l, \dots, \sigma_N\rangle \\
&= \sum_{k < l} 2\Delta_{kl}^* \delta_{\sigma_k, -} \delta_{\sigma_l, -} (-1)^{p_{k+1, l}} |\sigma_1, \dots, +, \dots, +, \dots, \sigma_N\rangle.
\end{aligned} \tag{A18}$$

Joining all these results finally gives the matrix elements

$$\begin{aligned}
&\langle \sigma'_1, \dots, \sigma'_k, \dots, \sigma'_l, \dots, \sigma'_N | H_{FF} | \sigma_1, \dots, \sigma_k, \dots, \sigma_l, \dots, \sigma_N \rangle \\
&= \left[ \left( \sum_{k=1}^N h_{kk} (\delta_{\sigma_k, -} - \delta_{\sigma_k, +}) \right) \delta_{\sigma'_k, \sigma_k} \delta_{\sigma'_l, \sigma_l} \right. \\
&\quad + \sum_{k < l} 2(-1)^{p_{k+1, l}} \left( (h_{kl} \delta_{\sigma_k, +} \delta_{\sigma_l, -} \delta_{\sigma'_k, -} \delta_{\sigma'_l, +} + h_{kl}^* \delta_{\sigma_k, -} \delta_{\sigma_l, +} \delta_{\sigma'_k, +} \delta_{\sigma'_l, -} \right. \\
&\quad \left. \left. + \Delta_{kl} \delta_{\sigma_k, +} \delta_{\sigma_l, +} \delta_{\sigma'_k, -} \delta_{\sigma'_l, -} + \Delta_{kl} \delta_{\sigma_k, -} \delta_{\sigma_l, -} \delta_{\sigma'_k, +} \delta_{\sigma'_l, +} \right) \right] \prod_{m \neq k, l} \delta_{\sigma'_m, \sigma_m}.
\end{aligned} \tag{A19}$$

The unitary matrix is obtained by

$$U_{FF} = e^{-iH_{FF}}, \tag{A20}$$

with  $H_{FF}$  computed through Eq. (A19).

The random quadratic Hamiltonian is obtained as follows. We can write Eq. (A7) in terms of Majorana fermions

$$\gamma = VC, \quad V = \frac{1}{\sqrt{2}} \begin{pmatrix} \mathbb{I} & \mathbb{I} \\ -i\mathbb{I} & i\mathbb{I} \end{pmatrix}. \tag{A21}$$

In this basis, the first quantized Hamiltonian  $\mathbf{H}_{\text{Majo}} = V\mathbf{H}V^\dagger$  is a purely imaginary antisymmetric matrix. Therefore,  $u = e^{i\mathbf{H}_{\text{Majo}}}$  belongs to the special orthogonal (SO) group. Hence:

1. Generate  $u \in \text{SO}(2L)$ .
2. Obtain  $\mathbf{H}_{\text{Majo}} = i \log u$ .
3. Transform it to complex fermions  $\mathbf{H} = V^\dagger \mathbf{H}_{\text{Majo}} V$ , and identify  $h$  and  $\Delta$ .
4. Use Eq. (A19).

## Appendix B: Fidelity cannot detect the loss of integrability

In this section, we show that the average fidelity is not sensitive to the regular or chaotic nature of the faultless unitary evolution. To do so, we will first write an expression of the fidelity, then we shall rewrite it in a convenient form to prove that the left-right invariance of the Haar measure is behind this insensitivity.

The outcome state of the faultless circuit is

$$|\Psi\rangle = U_T U_{T-1} \cdots U_1 |\psi_0\rangle, \quad (\text{B1})$$

where  $U_\tau$  is the unitary layer at time  $\tau$ , that can be structured or unstructured, fixed or sampled independently. The dissipative circuit produces a mixed state

$$\rho = \Phi(\Phi(\dots\Phi(|\psi_0\rangle\langle\psi_0|))) = \sum_{\mu_1, \dots, \mu_T=0}^r \prod_{\tau=1}^{\overleftarrow{T}} \hat{K}_{\mu_\tau} |\psi_0\rangle\langle\psi_0| \prod_{\tau=1}^{\overrightarrow{T}} \hat{K}_{\mu_\tau}^\dagger, \quad (\text{B2})$$

where we implement  $T$  times the quantum channel  $\Phi(\rho_\tau)$  which is given by the *diluted unitary*

$$\Phi(\rho_{\tau+1}) = \sum_{\mu_{\tau+1}=0}^r \hat{K}_{\mu_{\tau+1}} \rho_\tau \hat{K}_{\mu_{\tau+1}}^\dagger, \quad (\text{B3})$$

where

$$\hat{K}_0 = \sqrt{1-\kappa} U, \quad \text{verifying} \quad U^\dagger \tilde{U} = \mathbb{1}, \quad (\text{B4})$$

$$\hat{K}_{\mu \neq 0} = \sqrt{\kappa} K_\mu, \quad \text{verifying} \quad \sum_{\mu=1}^r K_\mu^\dagger K_\mu = \mathbb{1} \quad (\text{B5})$$

for  $\kappa \in [0, 1]$ . We are interested in computing the average of the fidelity

$$\mathcal{F} = \langle \Psi | \rho | \Psi \rangle. \quad (\text{B6})$$

To do so, it is useful to use the vectorized notation:

$$\|\psi\phi\rangle = |\psi\rangle \otimes |\phi^T\rangle \quad (\text{B7})$$

Equipped with it, we can write the fidelity in the 4-copy Hilbert space  $\mathcal{H}(2^{4L})$ :

$$\begin{aligned} \mathcal{F} &= \langle \Psi | \rho | \Psi \rangle \\ &= \langle \psi_0 | \left( \prod_{\tau=1}^{\overrightarrow{T}} U_\tau^\dagger \right) \left[ \sum_{\mu_1, \dots, \mu_T=0}^r \left( \prod_{\tau=1}^{\overleftarrow{T}} \hat{K}_{\mu_\tau} \right) |\psi_0\rangle\langle\psi_0| \left( \prod_{\tau=1}^{\overrightarrow{T}} \hat{K}_{\mu_\tau}^\dagger \right) \right] \left( \prod_{\tau=1}^{\overleftarrow{T}} U_\tau \right) |\psi_0\rangle \\ &= \sum_{\mu} \sum_{\mathbf{n}\mathbf{m}} \langle \psi_0 | \left( \prod_{\tau=1}^{\overrightarrow{T}} U_\tau^\dagger \right) | \mathbf{m} \rangle \langle \mathbf{m} | \left( \prod_{\tau=1}^{\overleftarrow{T}} \hat{K}_{\mu_\tau} \right) |\psi_0\rangle\langle\psi_0| \left( \prod_{\tau=1}^{\overrightarrow{T}} \hat{K}_{\mu_\tau}^\dagger \right) | \mathbf{n} \rangle \langle \mathbf{n} | \left( \prod_{\tau=1}^{\overleftarrow{T}} U_\tau \right) |\psi_0\rangle \\ &= \sum_{\mu} \sum_{\mathbf{n}\mathbf{m}} \langle \psi_0 \mathbf{m} \psi_0 \mathbf{n} | \left( \prod_{\tau=1}^{\overrightarrow{T}} U_\tau^\dagger \right) \otimes \left( \prod_{\tau=1}^{\overleftarrow{T}} \hat{K}_{\mu_\tau} \right) \otimes \left( \prod_{\tau=1}^{\overrightarrow{T}} \hat{K}_{\mu_\tau}^\dagger \right) \otimes \left( \prod_{\tau=1}^{\overleftarrow{T}} U_\tau \right) | \mathbf{m} \psi_0 \mathbf{n} \psi_0 \rangle \\ &= \sum_{\mu} \sum_{\mathbf{n}\mathbf{m}} \langle \mathbf{m} \mathbf{n} \mathbf{n} \mathbf{m} | \left( \prod_{\tau=1}^{\overleftarrow{T}} \hat{K}_{\mu_\tau} \right) \otimes \left( \prod_{\tau=1}^{\overrightarrow{T}} \hat{K}_{\mu_\tau}^\dagger \right)^T \otimes \left( \prod_{\tau=1}^{\overleftarrow{T}} U_\tau \right) \otimes \left( \prod_{\tau=1}^{\overrightarrow{T}} U_\tau^\dagger \right)^T | \psi_0 \psi_0 \psi_0 \psi_0 \rangle \\ &= \sum_{\mu} \sum_{\mathbf{n}\mathbf{m}} \langle \mathbf{m} \mathbf{n} \mathbf{n} \mathbf{m} | \prod_{\tau=1}^{\overleftarrow{T}} \left( \hat{K}_{\mu_\tau} \otimes \hat{K}_{\mu_\tau}^* \otimes U_\tau \otimes U_\tau^* \right) | \psi_0 \psi_0 \psi_0 \psi_0 \rangle \\ &= \frac{1}{d} \sum_{\mathbf{l}\mathbf{n}\mathbf{m}} \langle \mathbf{m} \mathbf{n} \mathbf{n} \mathbf{m} | \prod_{\tau=1}^{\overleftarrow{T}} \left( (1-\kappa) U_\tau \otimes U_\tau^* \otimes U_\tau \otimes U_\tau^* + \kappa \sum_{\mu_\tau=1}^r K_{\mu_\tau} \otimes K_{\mu_\tau}^* \otimes U_\tau \otimes U_\tau^* \right) | \mathbf{l}\mathbf{l}\mathbf{l}\mathbf{l} \rangle, \quad (\text{B8}) \end{aligned}$$

where

$$\sum_{\mathbf{n}} |\mathbf{n}\rangle = \left( \sum_{m=0,1} |m\rangle \right)^{\otimes L}, \quad (\text{B9})$$

and  $\boldsymbol{\mu} = (\mu_T, \dots, \mu_1)$  with  $\mu_\tau = 0, \dots, r$ . Observe that in the last equality we have further averaged over the computational basis

$$|\psi_0\psi_0\psi_0\psi_0\rangle \rightarrow \frac{1}{d} \sum_l ||l\rangle.$$

$$\mathcal{F} = \frac{1}{d} \left\langle +^{14;23} \left\| \prod_{\tau=1}^{\overleftarrow{T}} \left( (1-\kappa)\mathcal{U}_\tau + \kappa\mathcal{K}_\tau \right) \right\| +^{1234} \right\rangle, \quad \begin{cases} \left\| +^{14;23} \right\rangle &= \sum_{nm} ||mnmm\rangle \\ \mathcal{U}_\tau &= U_\tau \otimes U_\tau^* \otimes U_\tau \otimes U_\tau^* \\ \mathcal{K}_\tau &= \sum_{\mu_\tau=1}^r K_{\mu_\tau} \otimes K_{\mu_\tau}^* \otimes U_\tau \otimes U_{*\tau} \\ \left\| +^{1234} \right\rangle &= \sum_l ||l\rangle \end{cases} \quad (\text{B10})$$

Then, the fidelity can be written as:

$$\begin{aligned} \mathcal{F} &= \frac{1}{d} \left\langle +^{14;23} \left\| \prod_{\tau=1}^{\overleftarrow{T}} \mathcal{U}_\tau \prod_{\tau=1}^{\overleftarrow{T}} \left( (1-\kappa)\mathbb{1} + \kappa \prod_{\tau'=1}^{\overrightarrow{\tau}} \mathcal{U}_{\tau'}^\dagger \mathcal{K}_\tau \prod_{\tau''=1}^{\overleftarrow{\tau-1}} \mathcal{U}_{\tau''} \right) \right\| +^{1234} \right\rangle \\ &= \frac{1}{d} \left\langle +^{14;23} \left\| \mathcal{U}(T, 1) \prod_{\tau=0}^{T-1} \left( (1-\kappa)\mathbb{1} + \kappa \mathcal{U}^\dagger(T-\tau, 1) \mathcal{K}_{T-\tau} \mathcal{U}(T-1-\tau, 1) \right) \right\| +^{1234} \right\rangle, \end{aligned} \quad (\text{B11})$$

where we used

$$\prod_{\tau'}^{\overrightarrow{\tau}} \mathcal{U}_{\tau'} \equiv \mathcal{U}(\tau, \tau'). \quad (\text{B12})$$

Equation (B11) can be easily proved by induction. Consider the case  $T = 2$ :

$$\begin{aligned} \mathcal{F} &= \frac{1}{d} \left\langle +^{14;23} \left\| \left( (1-\kappa)\mathcal{U}_2 + \kappa\mathcal{K}_2 \right) \left( (1-\kappa)\mathcal{U}_1 + \kappa\mathcal{K}_1 \right) \right\| +^{1234} \right\rangle \\ &= \frac{1}{d} \left\langle +^{14;23} \left\| \mathcal{U}_2 \left( (1-\kappa)\mathcal{U}_1 + \kappa\mathcal{U}_2^\dagger \mathcal{K}_2 \mathcal{U}_1 \right) \left( (1-\kappa) + \kappa\mathcal{U}_1^\dagger \mathcal{K}_1 \right) \right\| +^{1234} \right\rangle \\ &= \frac{1}{d} \left\langle +^{14;23} \left\| \mathcal{U}_2 \mathcal{U}_1 \left( (1-\kappa)\mathbb{1} + \kappa\mathcal{U}_1^\dagger \mathcal{U}_2^\dagger \mathcal{K}_2 \mathcal{U}_1 \right) \left( (1-\kappa)\mathbb{1} + \kappa\mathcal{U}_1^\dagger \mathcal{K}_1 \right) \right\| +^{1234} \right\rangle. \end{aligned} \quad (\text{B13})$$

Then, the case  $T - 1$  is

$$\mathcal{F} = \frac{1}{d} \left\langle +^{14;23} \left\| \mathcal{U}(T-1, 1) \prod_{\tau=0}^{T-2} \left( (1-\kappa)\mathbb{1} + \kappa \mathcal{U}^\dagger(T-1-\tau, 1) \mathcal{K}_{T-1-\tau} \mathcal{U}(T-2-\tau, 1) \right) \right\| +^{1234} \right\rangle \quad (\text{B14})$$

and the case  $T$  is

$$\begin{aligned} \mathcal{F} &= \frac{1}{d} \left\langle +^{14;23} \left\| \left( (1-\kappa)\mathcal{U}_T + \kappa\mathcal{K}_T \right) \mathcal{U}(T-1, 1) \prod_{\tau=0}^{T-2} \left( (1-\kappa)\mathbb{1} + \kappa \mathcal{U}^\dagger(T-1-\tau, 1) \mathcal{K}_{T-1-\tau} \mathcal{U}(T-2-\tau, 1) \right) \right\| +^{1234} \right\rangle \\ &= \frac{1}{d} \left\langle +^{14;23} \left\| \mathcal{U}_T \mathcal{U}(T-1, 1) \left( (1-\kappa)\mathbb{1} + \kappa \mathcal{U}^\dagger(T-1, 1) \mathcal{K}_T \mathcal{U}(T-1, 1) \right) \right. \right. \\ &\quad \left. \left. \times \prod_{\tau=0}^{T-2} \left( (1-\kappa)\mathbb{1} + \kappa \mathcal{U}^\dagger(T-1-\tau, 1) \mathcal{K}_{T-1-\tau} \mathcal{U}(T-2-\tau, 1) \right) \right\| +^{1234} \right\rangle. \end{aligned} \quad (\text{B15})$$

Equation (B11) is quite advantageous since

$$\left\langle +^{14;23} \left\| \mathcal{U}(T, 1) \right. \right\rangle = \left\langle +^{14;23} \right\|. \quad (\text{B16})$$

To see this, we undo the vectorization:

$$\begin{aligned}
\langle +^{14;23} \| \mathcal{U}(T, 1) &= \sum_{nm} \langle mnnm \| \left( U(T, 1) \otimes U^*(T, 1) \otimes U(T, 1) \otimes U^*(T, 1) \right) \\
&= \sum_{nm} \langle mmnn \| \left( U(T, 1) \otimes U^*(T, 1) \otimes U(T, 1) \otimes U^*(T, 1) \right) \\
&= \sum_{nm} \left( U^\dagger(T, 1) \otimes U^T(T, 1) \otimes U(T, 1)^\dagger \otimes U^T(T, 1) \| mmnn \right)^\dagger \\
&= \sum_{nm} \left( U^\dagger(T, 1) |m\rangle \langle m| U(T, 1) \otimes U^\dagger(T, 1) |n\rangle \langle n| U(T, 1) \right)^\dagger \\
&= (\mathbb{1} \otimes \mathbb{1})^\dagger = \sum_{mn} \langle mmnn \| = \sum_{mn} \langle mnnm \| = \langle +^{14;23} \|,
\end{aligned} \tag{B17}$$

where we have exchanged copies 2 and 4. Hence, we write the fidelity as

$$\mathcal{F} = \frac{1}{d} \langle +^{14;23} \| \prod_{\tau=0}^{T-1} \left( (1-\kappa)\mathbb{1} + \kappa \mathcal{U}^\dagger(T-\tau, 1) \mathcal{K}_{T-\tau} \mathcal{U}(T-1-\tau, 1) \right) \| +^{1234} \rangle \tag{B18}$$

We are now ready to take the average of the quantity above, and it is easy to see that it involves products of the object

$$\begin{aligned}
\tilde{\mathcal{K}}_{T-\tau} &\equiv \overline{\mathcal{U}^\dagger(T-\tau, 1) \mathcal{K}_{T-\tau} \mathcal{U}(T-1-\tau, 1)} \\
&= \sum_{\mu_{T-\tau}=1}^r \overline{U^\dagger(T-\tau, 1) K_{\mu_{T-\tau}} U(T-\tau, 1) \otimes U(1, T-\tau) K_{\mu_{T-\tau}}^* U^*(T-1-\tau, 1)} \\
&\quad \overline{U^\dagger(T-\tau, 1) U_{T-\tau} U(T-1-\tau, 1) \otimes U^T(T-\tau, 1) U_{T-\tau}^* U^*(T-1-\tau, 1)} \\
&= \sum_{\mu_\tau=1}^r \overline{U^\dagger(T-\tau, 1) K_{\mu_{T-\tau}} U(T-\tau, 1) \otimes U(1, T-\tau) K_{\mu_{T-\tau}}^* U^*(T-1-\tau, 1)} \otimes \mathbb{1} \otimes \mathbb{1}.
\end{aligned} \tag{B19}$$

Since the Kraus operators  $K_\mu$  are chopped from a large  $rd \times rd$  unitary matrix sampled according to the Haar measure, each of them inherits its properties, in particular, the fundamental left-right invariance. Because of this,

$$\overline{U^\dagger(T-\tau, 1) K_{\mu_\tau} U(T-\tau, 1) \otimes U(1, T-\tau) K_{\mu_\tau}^* U^*(T-1-\tau, 1)} = \overline{K_{\mu_\tau} \otimes K_{\mu_\tau}^*}. \tag{B20}$$

The Weingarten calculus [36] allows us to compute the average over the two copies of the Kraus operators:

$$\overline{K_{\mu_\tau} \otimes K_{\mu_\tau}^*} = \frac{1}{dr} \sum_{mn} \|mm\rangle \langle nn\|, \tag{B21}$$

because  $(\overline{K_{\mu_\tau} \otimes K_{\mu_\tau}^*})^\tau = 1/r^{\tau-1} \overline{K_{\mu_\tau} \otimes K_{\mu_\tau}^*}$ ,  $\tilde{\mathcal{K}}$  is a projector. Then, it can be seen that

$$\left( (1-\kappa)\mathbb{1} + \kappa \tilde{\mathcal{K}} \right)^T = (1-\kappa)^T \mathbb{1} + (1 - (1-\kappa)^T) \tilde{\mathcal{K}}. \tag{B22}$$

Finally, computing the overlaps  $\langle +^{14;23} \| +^{1234} \rangle = d$  and

$$\langle +^{14;23} \| \tilde{\mathcal{K}} \| +^{1234} \rangle = r \frac{1}{dr} \sum_{mm'm'n'u'} \langle mnnm \| \left( \|m'm'l'l'\rangle \langle n'n'l'l'\| \right) \|uuu\rangle = 1, \tag{B23}$$

we obtain the final result:

$$\mathcal{F} = \frac{1}{d} + (1-\kappa)^T \left( 1 - \frac{1}{d} \right). \tag{B24}$$

Notice that this expression only depends on the dissipation parameter  $\kappa$ , indicating that neither the rank  $r$  nor the structure of the clean circuit influences the decay of fidelity.



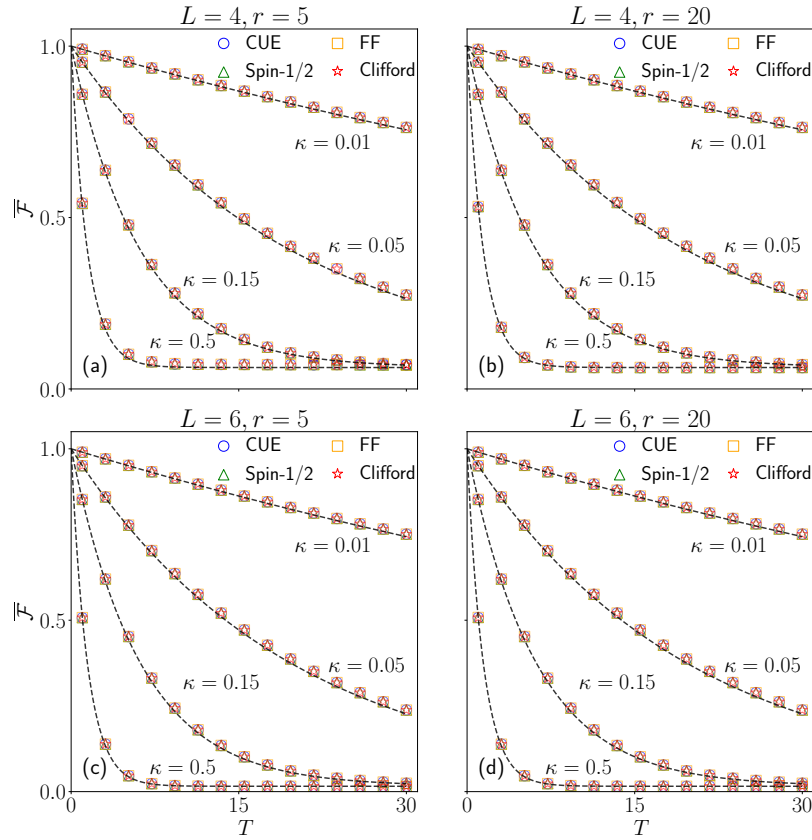


Figure SM1. Fidelity decay after applying faulty quantum maps considering different models for different values of  $\kappa$ , system size, and Kraus rank (see caption for the values). The dashed line represents the fidelity decay of Eq. (B24).

We now numerically show that the fidelity does not depend on the model considered and that it follows Eq. (B24). We consider a random quantum circuit where in each layer we apply a different diluted unitary, corresponding to a  $d^2 \times d^2$  matrix, sampled randomly within the same model. The initial state is the faultless pure state  $|\Psi_0\rangle = |0\rangle^{\otimes L}$ . We measure the fidelity between the ideal closed evolution with  $\kappa = 0$  and an imperfect map realization with  $\kappa \neq 0$ . The average fidelity is computed for several values of  $\kappa$  and  $r$ .

In Fig. SM1 (a) we plot the average fidelity as a function of the number of layers  $T$  for the four classes of maps considered in the main text, with  $\kappa = 0.01, 0.05, 0.15, 0.5$ , fixed rank  $r = 5$ , and  $L = 4$ . In Fig. SM1 (b) we repeat the process but now with  $r = 20$ . Finally, Figs. SM1 (c) and (d) represent the same as Figs. SM1 (a) and (b), respectively, but with  $L = 6$ . From Figs. SM1 (a) and (b), we observe that the fidelity decay is the same for the four maps considered, even for small values of  $\kappa$  and  $r$ , and is well captured by Eq. (B24). This is surprising not only because we cannot distinguish between the behavior of the four maps generated by non-universal gates, but also because their fidelity is the same as in the case of unitaries belonging to the CUE, which is a random ensemble that generates generic dynamics. Furthermore, the rank measures the number of ways the environment interacts with the system; hence, this result is even more peculiar since we observe that, no matter how the environment perturbs the system, the effects on the fidelity will be, on average, the same. Finally, the results from Figs. SM1 (c) and (d) show that the equality of fidelity decay is also observed for other system sizes.

It is thus safe to conclude that fidelity decay is not a good measure of quantum chaos, as it is blind to the degree of non-unitarity of different maps. More boldly, we can claim that the average fidelity has a universal behavior.

### Appendix C: Robustness of ring-to-disk transition

In this section, we provide numerical evidence of the ring-to-disk robustness that motivated some of the results in the main text.

In the main text, we argued that integrable models with degeneracies undergo two transitions, a cluster-to-ring (C-R)

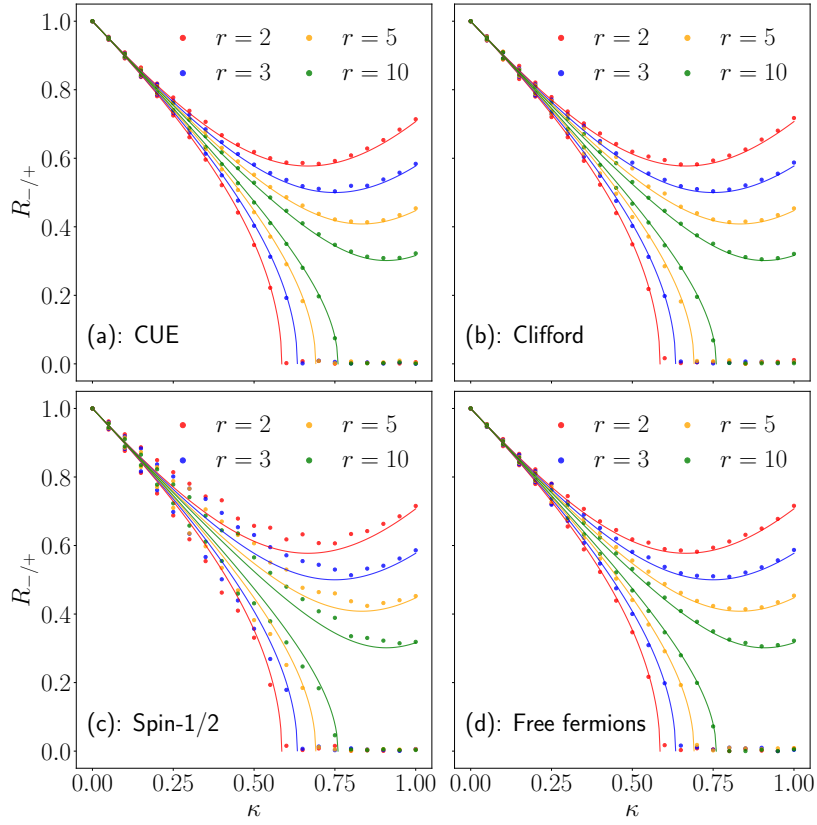


Figure SM2. Inner and outer radius,  $R_-$  and  $R_+$ , of the quantum map Eq. (1) with a unitary drawn from the (a) CUE, (b) Clifford group, (c) Integrable spin-1/2, and (d) free fermions ensemble for  $L = 6$  and different  $r$ . The dots represent numerical points obtained with a random map sampled each time for distinct  $r$ , and the lines the theoretical prediction of Eq. (2).

followed by a ring-to-disk (R-D). This was observed through the spectrum of maps with unitaries taken from different ensembles. However, it was also mentioned that before the C-R transition, the absolute value of the eigenvalues would have minimum and maximum radius approximately given by Eq. (2).

In Figs. SM2 (a)–(d) we show that Eq. (2) is valid for the models we considered. The data points were obtained by sampling a random map for each value of  $r$ . We see that even considering a single map, the data matches well the prediction. The case of the spin-1/2 chain seems to be the one that deviates the most from the prediction. However, by inspecting the spectrum of Fig. 1, we see the formation of a cluster in the vicinity of the positive real axis, which can lead to some points having an absolute value larger than  $R_+$ . Nevertheless, the prediction for  $R_-$  matches the expected one very well, especially for  $\kappa \approx \kappa_{\text{R-D}}$ .

These results have two major implications: first, it means that the R-D transition value is approximately the same for all the models; second, it is approximately true that the radius of the clusters is  $R = (R_+ - R_-)/2$ , and that their centers are in the circumference of radius  $D = (R_+ + R_-)/2$ , as assumed in the main text.